

Diffuse scattering of x rays at grazing angles from near-surface defects in crystals

S. Grotehans, G. Wallner, E. Burkel, H. Metzger, J. Peisl, and H. Wagner

Ludwig-Maximilians-Universität München, D-8000 München 22, Federal Republic of Germany

(Received 23 August 1988)

We derive the cross section for the intensity of diffuse x-ray scattering under conditions of grazing incidence and exit in the vicinity of Bragg reflections induced by near-surface defects. The theoretical results for a simple model are compared with first measurements on Si single crystals implanted with 80-keV As ions. Reasonable agreement is obtained for a profile of a defect distribution corresponding to that of the collision energy deposited by the implanted ions.

I. INTRODUCTION

Lattice distortions caused by impurities, vacancies, and interstitials in real crystals give rise to a diffuse scattering of x rays which carries detailed information on the location, symmetry, and strength of such defects. In particular, the long-ranged part of the static displacements leads to a strongly enhanced diffuse intensity in the vicinity of the Bragg peaks which is called Huang scattering.

In the past, measurements of the Huang scattering have been made primarily on simple systems with randomly distributed defects at low concentration to study lattice distortions in the bulk of materials.¹ In this paper we extend the method to investigate defect configurations near the surface of crystals.

The confinement of x-ray scattering to a subsurface layer is achieved by employing grazing incidence or exit angles. In this diffraction scheme the width of the illuminated layer is controlled by the penetration depth of the interior evanescent wave associated with total reflection.² Following first experiments,^{3,4} several experimental investigations of the near-surface structure of solids have been reported (e.g., Refs. 5–7), where Bragg diffraction under condition of grazing incidence *and* exit was observed. In Sec. II the expression for the cross section of the surface-specific Huang scattering is derived. In Sec. III we describe a first experiment on a Si crystal implanted with As ions and in Sec. IV we compare the result with the theoretical predictions.

This investigation demonstrates that surface Huang scattering can be employed to yield depth-resolved information on the near-surface defect distribution in a non-destructive way.

II. THE CROSS SECTION OF SURFACE DIFFUSE HUANG SCATTERING

We consider a plane electromagnetic wave $\mathbf{E}_i(\mathbf{R}, t) = \mathbf{E}_i \exp[i(\mathbf{K}_i \cdot \mathbf{R} - \omega t)]$ incident upon the plane surface of a crystalline material with an average index of refraction $n = 1 - (2\pi r_e^2 \bar{\rho} / K_i^2)$, where $r_e = e^2 / mc^2$ and $\bar{\rho}$ denotes the spatially averaged electronic density in the pure crystal. The sample occupies the half-space $z > 0$. The refracted wave $\bar{\mathbf{E}}_i(\mathbf{R}, t)$ propagates in the sample with a wave vector $\bar{\mathbf{K}}_i$, $|\bar{\mathbf{K}}_i| = \bar{K}_i = nK_i$, and is scattered

by the inhomogeneity $\bar{\rho}(\mathbf{R}) \equiv \rho(\mathbf{R}) - \bar{\rho}$ in the electronic density $\rho(\mathbf{R})$.

In a perfect crystal the lattice periodicity of $\rho(\mathbf{R})$ leads to a dynamic coupling among interior beams having wave vectors which differ by a reciprocal-lattice vector. According to the dynamic diffraction theory this coupling is only effective in a narrow angular region (Darwin region) where it describes the structure of the Bragg-reflected intensity.^{8,9} Here we are concerned with the diffuse scattering induced by randomly distributed impurities which arises in the vicinity of the Bragg reflections but well outside of the Darwin regime. Therefore, a kinematical description employing the first Born approximation for the scattering of a single incident albeit refracted beam should be sufficiently accurate. In this approach the scattering cross section is given by²

$$\frac{d\sigma}{d\Omega} = r_e^2 a_{fi} \langle |\Gamma(\bar{\mathbf{Q}})|^2 \rangle, \quad (1)$$

where $\bar{\mathbf{Q}} \equiv \bar{\mathbf{K}}_i - \bar{\mathbf{K}}_f$ and

$$\Gamma(\bar{\mathbf{Q}}) = \int d^3R e^{i\bar{\mathbf{Q}} \cdot \mathbf{R}} \bar{\rho}(\mathbf{R}). \quad (2)$$

The average of $\Gamma(\bar{\mathbf{Q}})$ in (1) is a thermal average as well as an average over the distribution of the defects. The geometrical factor a_{fi} will be specified later; it depends on the polarization of the incident beam and includes transmission coefficients arising from the refraction of the incoming and the elastically scattered outgoing waves at the sample surface. The scattering geometry is shown in Fig. 1. We split vectors into their two-component lateral part and their z component perpendicular to the surface so that $\mathbf{R} = (\mathbf{r}, z)$ and $\bar{\mathbf{Q}} = (\mathbf{k}_i - \mathbf{k}_f, \kappa)$ with the vertical component

$$\begin{aligned} \kappa &= [(Kn)^2 - k_i^2]^{1/2} + [(Kn)^2 - k_f^2]^{1/2} \\ &= K [(\sin^2 \alpha_i - \sin^2 \alpha_c)^{1/2} + (\sin^2 \alpha_f - \sin^2 \alpha_c)^{1/2}], \end{aligned} \quad (3)$$

where $K = \omega/c$. In (3), α_c denotes the critical angle for total external reflection as determined by $\sin^2 \alpha_c = 1 - n^2$. Since $n < 1$, the z component κ becomes complex with $\text{Im}\kappa > 0$ if $\alpha_i < \alpha_c$ or $\alpha_f < \alpha_c$. In such cases the z integration in Γ is practically confined to a surface layer of depth $\approx (\text{Im}\kappa)^{-1}$ which is typically of the order of 50–100 Å. As long as $\bar{\mathbf{Q}} \neq 0$, $\bar{\rho}(\mathbf{R})$ may be replaced by

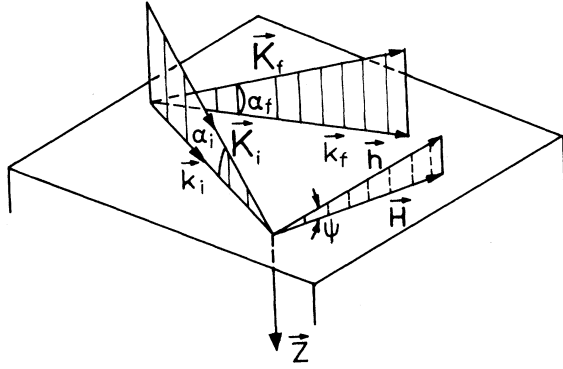


FIG. 1. Diffraction geometry. Incident (\mathbf{K}_i) and diffracted (\mathbf{K}_f) beam wave vector. The specular beam is not shown. The reciprocal-lattice vector \mathbf{H} is perpendicular to the (220) planes of a single crystal. The (220) planes make an tilt angle Ψ with the normal surface vector. Ψ is defined by $\sin\Psi = H_z/|\mathbf{H}|$.

$\rho(\mathbf{R})$ which is a superposition of localized electronic charge densities

$$\rho(\mathbf{R}) = \sum_m \rho_m(\mathbf{R} - \mathbf{R}_m - \delta\mathbf{U}_m). \quad (4)$$

The displacements $\delta\mathbf{U}_m \equiv \mathbf{U}_m - \langle \mathbf{U}_m \rangle$ from the equilibrium lattice positions \mathbf{R}_m in the reference lattice are due to thermal phonons and static fluctuations of the internal stress caused by the defects.

With $\rho(\mathbf{R})$ from (4) we have

$$\Gamma(\bar{\mathbf{Q}}) = \sum_m F_m(\bar{\mathbf{Q}}) e^{i\bar{\mathbf{Q}} \cdot (\mathbf{R}_m + \delta\mathbf{U}_m)}, \quad (5)$$

where $F_m(\bar{\mathbf{Q}})$ is the atomic scattering factor. We assume that the thermal average and the average over the defect distribution factorize, which holds strictly in a harmonic lattice. The former yields thermal Debye-Waller factors which we absorb in $F_m(\bar{\mathbf{Q}})$ and a thermal diffuse scattering. Since we focus attention on distortion scattering, we may eliminate the thermal contribution by subtracting the diffuse intensity of a defect-free sample. For the defect-induced displacements, denoted by \mathbf{U}_m^D , we employ the usual linear superposition

$$\mathbf{U}_m^D = \sum_s \mathbf{G}_m^s \tau_s, \quad (6)$$

where the sum runs over defect sites \mathbf{R}_s and $\tau_s = 0, 1$ are occupation numbers with $\langle \tau_s \rangle = c_s$, the local concentration of defects. Similarly, we have

$$F_m(\bar{\mathbf{Q}}) = F_m^0(\bar{\mathbf{Q}}) \left[1 + \sum_s f_m^s \tau_s \right] \quad (7)$$

for the dependence of F_m upon defects. The form factors F_m^0 of the defect-free lattice will also be inhomogeneous because of the near-surface relaxation in the lattice positions.

Our basic assumption is that the defects are distributed independently with a small concentration $c_s \ll 1$. The average on the configurations $\{\tau_s\}$ can then be carried out straightforwardly, as for bulk scattering,^{1,10} with the

result

$$\langle |\Gamma|^2 \rangle - |\langle \Gamma \rangle|^2 = \sum_s c_s |A_s|^2, \quad (8)$$

$$A_s = F_s^D e^{i\bar{\mathbf{Q}} \cdot \mathbf{R}_s} + \sum_m e^{-M_m} \langle F_m \rangle (i\bar{\mathbf{Q}} \cdot \mathbf{G}_m^s - V_m^s) e^{i\bar{\mathbf{Q}} \cdot \mathbf{R}_m},$$

with the static Debye-Waller exponent

$$M_m(\bar{\mathbf{Q}}) = \sum_s c_s [f_m^s + V(\bar{\mathbf{Q}})_m^s] \quad (9)$$

and

$$V_m^s(\bar{\mathbf{Q}}) = 1 + i\bar{\mathbf{Q}} \cdot \mathbf{G}_m^s - (1 + f_m^s) \exp(i\bar{\mathbf{Q}} \cdot \mathbf{G}_m^s). \quad (10)$$

For the sake of completeness the direct (Laue-) scattering from defects with amplitudes F_s^D has been introduced, although its contribution is negligible if $c_s \ll 1$. Likewise, the Debye-Waller factor $\exp(-M_m)$ may be replaced by unity, provided the sum in (9) converges, which holds for pointlike defects and compact clusters but excludes extended line defects.¹⁰

We specialize now for diffuse scattering near a Bragg reflection with reciprocal-lattice vector $\mathbf{H} = (\mathbf{h}, 0)$ lying parallel to the surface. Thus $\bar{\mathbf{Q}} = (\mathbf{h} + \mathbf{q}, \kappa) \equiv \mathbf{Q} + \mathbf{h}$. If $H_z \neq 0$, then κ must be replaced by $\kappa - H_z$.

The leading singular term in the cross section for $\mathbf{q} \rightarrow 0$ arises from the long-distance behavior of $\mathbf{G}_m^s \sim |\mathbf{R}_m - \mathbf{R}_s|^{-2}$. This contribution is subtracted in $V_m^s(\bar{\mathbf{Q}})$, which only contains short-range parts. As a further simplification we neglect surface effects in F_m and M_m by setting $\langle F_m(\bar{\mathbf{Q}}) \rangle \exp[-M_m(\bar{\mathbf{Q}})] \approx \bar{F}(\mathbf{h})$. Hence, for small q values and after neglecting the Laue term we arrive at

$$A_s \approx e^{i\mathbf{q} \cdot \mathbf{r}_s} \frac{\bar{F}(\mathbf{h})}{v_c} \int d^2r \int_0^\infty dz i\bar{\mathbf{Q}} \cdot \mathbf{G}(\mathbf{r}, z, z_s) e^{i\mathbf{q} \cdot \mathbf{r}} e^{i\kappa z}$$

$$= e^{i\mathbf{q} \cdot \mathbf{r}_s} \frac{\bar{F}(\mathbf{h})}{v_c} i\bar{\mathbf{Q}} \cdot \tilde{\mathbf{G}}(\mathbf{Q}|z_s). \quad (11)$$

In (11) we employed the translational symmetry in lateral directions and the continuum approximation for lattice sums, with v_c denoting the volume of the unit cell. A further discussion of this approximation is given later [following Eq. (21)].

Substituting (11) into (8) we obtain ultimately

$$\sum_s c_s |A_s|^2 \approx \mathcal{F} \left| \frac{\bar{F}}{v_c} \right|^2 \int_0^\infty dz' \bar{\rho}_D(z') |\bar{\mathbf{Q}} \cdot \tilde{\mathbf{G}}(\mathbf{Q}|z')|^2, \quad (12)$$

with the illuminated surface area \mathcal{F} and the density of defects $\bar{\rho}_D(z) \equiv \langle \rho_D(\mathbf{R}) \rangle$. Equation (12) corresponds to the well-known expression for the Huang scattering in the bulk case.^{1,10} The modifications arise solely from the broken translational symmetry in the z direction perpendicular to the sample surface. In (12), $\bar{\rho}_D(z)$ describes the density profile of the defects. Likewise, the kernel $\tilde{\mathbf{G}}(\mathbf{Q}|z)$ varies with the depth z because of boundary conditions for the displacements at the surface $z = 0$.

As in the bulk case, the behavior of $\tilde{\mathbf{G}}(\mathbf{Q}|z)$ for values of \mathbf{q} which are small compared to inverse lattice distances may be obtained from continuum elasticity, whereby the

defects are represented by force dipoles. The internal stress tensor reads [$\mathbf{U}(\mathbf{R}) \equiv \mathbf{U}^D(\mathbf{R})$]

$$\sigma_{\alpha\beta} = C_{\alpha\beta\gamma\delta} \partial_\gamma U_\delta, \quad (13)$$

with the elastic constants $C_{\alpha\beta\gamma\delta}$. The mechanical equilibrium conditions are

$$\begin{aligned} \partial_\beta \sigma_{\alpha\beta}(\mathbf{R}) &= P_{\alpha\beta} \partial_\beta \rho_D(\mathbf{R}), \quad \mathbf{R} \in V \\ \hat{n}_\beta(\mathbf{R}) \sigma_{\alpha\beta}(\mathbf{R}) &= 0, \quad \mathbf{R} \in \partial V \end{aligned} \quad (14)$$

where we assume the surface (i.e., "boundary") of the sample, ∂V , with unit vector $\hat{\mathbf{n}}$ to be stress free. We take the defects to be pure dilation centers. Then the force-dipole tensor is diagonal, $P_{\alpha\beta} = P \delta_{\alpha\beta}$. The displacements obeying Eq. (14) may then be written in the continuum

version of (6):

$$\mathbf{U}(\mathbf{R}) = \int d^3 R' \mathbf{G}(\mathbf{R}; \mathbf{R}') \rho_D(\mathbf{R}'). \quad (15)$$

From (13) and (14) we infer that in the semi-infinite system

$$\begin{aligned} \partial_\beta \partial_\delta C_{\alpha\beta\gamma\delta} G_\gamma(\mathbf{R}; \mathbf{R}') &= P \partial_\alpha \delta(\mathbf{R} - \mathbf{R}'), \quad \mathbf{R}, \mathbf{R}' \in V \\ \partial_\delta C_{\alpha\beta\gamma\delta} G_\gamma(\mathbf{r}, 0; \mathbf{R}') &= 0, \quad \mathbf{R}' \in \partial V. \end{aligned} \quad (16)$$

In order to proceed analytically we finally simplify to an elastically isotropic material so that $C_{\alpha\beta\gamma\delta} = \lambda \delta_{\alpha\beta} \delta_{\gamma\delta} + \mu (\delta_{\alpha\gamma} \delta_{\beta\delta} + \delta_{\alpha\delta} \delta_{\beta\gamma})$. The solution of Eqs. (16) for the partial Fourier transform $\tilde{\mathbf{G}}(\mathbf{q}|z, z')$ can be obtained by standard methods and reads

$$\frac{2}{P} (\lambda + 2\mu) \tilde{\mathbf{G}}(\mathbf{q}|z, z') = \left[i \hat{\mathbf{q}} - \hat{\mathbf{z}} \frac{1}{q} \partial_z \right] e^{-q|z-z'|} + \left[i \hat{\mathbf{q}} \left[\frac{3\mu + \lambda}{\lambda + \mu} - 2zq \right] - \hat{\mathbf{z}} \left[\frac{3\mu + \lambda}{\lambda + \mu} + 2zq \right] \right] e^{-q(z+z')}. \quad (17)$$

The first term on the right-hand side of (17) gives $\tilde{\mathbf{G}}_\infty$ for the infinite medium, and the second term arises from the boundary condition of a stress-free plane surface at $z=0$. For Eq. (12) we need the additional Fourier-Laplace transform with respect to z , which is found as

$$-\frac{\lambda + 2\mu}{P} i \bar{\mathbf{Q}} \cdot \tilde{\mathbf{G}}(\mathbf{Q}|z') = e^{i\kappa z'} \left[\mathbf{h} \cdot \hat{\mathbf{q}} \frac{q}{q^2 + \kappa^2} + 1 \right] - e^{-qz'} \left[\mathbf{h} \cdot \hat{\mathbf{q}} \left[\frac{q}{q^2 + \kappa^2} + \frac{\mu(i\kappa - q) + i\kappa(\mu + \lambda)}{(\mu + \lambda)(i\kappa - q)^2} \right] + \frac{2i\kappa\mu + \lambda(i\kappa - q)}{(\mu + \lambda)(i\kappa - q)} \right]. \quad (18)$$

After collection of terms, the final result for the scattering cross section, which is proportional to the experimentally observed diffuse scattered intensity I_H , is

$$\begin{aligned} \frac{d\sigma}{d\Omega} &= \mathcal{F} r_e^2 a_{fi} \frac{|\bar{\mathbf{F}}(\mathbf{h})|^2}{v_c^2} S(\bar{\mathbf{Q}}), \\ S(\bar{\mathbf{Q}}) &= \int_0^\infty dz' |\bar{\mathbf{Q}} \cdot \tilde{\mathbf{G}}(\mathbf{Q}|z')|^2 \bar{\rho}_D(z'). \end{aligned} \quad (19)$$

For an incident wave with electric field polarized perpendicularly to the plane of incidence, the factor a_{fi} is given by²

$$a_{fi} = |T_i^\perp|^2 (|T_f^\perp|^2 \cos^2 2\theta + |T_f^\parallel|^2 \sin^2 2\theta \sin^2 \bar{\alpha}_f), \quad (20)$$

where $\cos 2\theta = \hat{\mathbf{k}}_i \cdot \hat{\mathbf{k}}_f$ and

$$\begin{aligned} T_{i,f}^\perp &= \frac{2 \sin \alpha_{i,f}}{\sin \alpha_{i,f} + n \sin \bar{\alpha}_{i,f}}, \\ T_f^\parallel &= \frac{2 \sin \alpha_f}{\sin \bar{\alpha}_f + n \sin \alpha_f}. \end{aligned} \quad (21)$$

The glancing angles are related through Snell's law, $\cos \alpha_{i,f} = n \cos \bar{\alpha}_{i,f}$.

Let us go back for a moment to Eq. (11), where we introduced a continuum approximation for lattice sums. Thereby we tacitly assumed the reference lattice to be homogeneous. This is not quite correct, since the laterally averaged defect distribution varies with depth z . The averaged displacement $\langle \mathbf{U}(\mathbf{R}) \rangle$ arising from $\bar{\rho}_D(z)$ may be estimated from Eqs. (13) and (14) for dilatation clus-

ters and with isotropic elastic constants. If we ignore stresses at the lateral edges of the sample we find $\langle \mathbf{U}(\mathbf{R}) \rangle = (0, 0, u_z(z))$ and

$$u_z(z) = \frac{P}{\lambda + 2\mu} \int_0^z dz' \bar{\rho}_D(z'). \quad (22)$$

In principle this lattice distortion leads to an inhomogeneous index of refraction $n(z)$ in the surface layer, where $\bar{\rho}_D(z) \neq 0$. However, the deviation of $n(z)$ from its bulk value n is numerically negligible: With $\bar{\rho}_D(z > l_D) = 0$, $l_D = O(10^{-5} \text{ cm})$, $P/(\lambda + 2\mu) = O(10^{-24} \text{ cm}^3)$, and $n_D = O(10^{14} \text{ cm}^{-2})$ for the number of defects per unit area as typical values for point defects in Si produced by ion implantation to a medium dose, we obtain $u_z(l_D) = O(10^{-10} \text{ cm})$ for the maximum displacement and average strain $\bar{\epsilon}_{zz} = O(10^{-5})$, yielding $|n(z) - n| = |n - 1| \bar{\epsilon}_{zz} = O(10^{-9})$.

It is instructive to evaluate (19) in the angular regime of total reflection ($\alpha_i < \alpha_c$ or $\alpha_f < \alpha_c$) for a constant density $\bar{\rho}_D(z) \equiv \bar{\rho}_D$ and to compare with the intensity for bulk Huang scattering. As we pointed out before, the scattered intensity in the case of $\text{Im}\kappa > 0$ comes from a surface layer whose depth can be controlled by variation of α_i and α_f . The leading term in $S(\bar{\mathbf{Q}})$ for $q \rightarrow 0$, $\text{Im}\kappa > 0$, is

$$\mathcal{F} S(\bar{\mathbf{Q}}) \sim \left[\frac{P}{\lambda + \mu} \right]^2 \frac{\bar{\rho}_D \mathcal{F}}{2q|\kappa|^2} |\mathbf{h} \cdot \hat{\mathbf{q}} + i\kappa|^2, \quad (23)$$

which predicts a q^{-1} singularity. This is in contrast to

the q^{-2} behavior of the bulk Huang scattering. The latter may also be obtained from (19) for angles $\alpha_i = -\alpha_f \gg \alpha_c$, i.e., $\kappa=0$, which formally yields an infinite penetration depth. Of course, we have to take into account absorption, which can be done simply by keeping a finite value of $(\text{Im}\kappa)^{-1}$ as determined by the absorption length. We then find for $\text{Re}\kappa \rightarrow 0$ and small q values that

$$\mathcal{F}S(\bar{Q}) \sim \left[\frac{P}{\lambda + 2\mu} \right]^2 N_D \frac{1}{q^2} |\mathbf{h} \cdot \hat{\mathbf{q}} + 1|^2, \quad (24)$$

where $N_D = \mathcal{F}\bar{\rho}_D / \text{Im}\kappa$ is the number of defects in the scattering volume.

In order to illustrate the angular dependence of the scattered diffuse intensity as given by (19) we discuss some \mathbf{q} scans chosen in view of the experimental situation. Let us consider the projections \mathbf{k}_i and \mathbf{k}_f of the exterior wave vectors \mathbf{K}_i and \mathbf{K}_f , starting in the Bragg position with $\alpha_i = \alpha_f < \alpha_c$ (see Fig. 2). After rotation of \mathbf{k}_f by the angle φ with fixed α_f , the resulting deviation from the Bragg reflection is \mathbf{q} ("q scan"). Simultaneous rotations of \mathbf{k}_i and \mathbf{k}_f by $-\varphi$ at fixed $\alpha_i = \alpha_f$ yields \mathbf{q}_\perp , being practically perpendicular to the reciprocal-lattice vector $\mathbf{H} = (\mathbf{h}, 0)$ for small values of $|\varphi|$ ("q_⊥ scan" or "ω scan"). Alternatively, $\mathbf{k}_i \rightarrow \mathbf{k}_i''$ and $\mathbf{k}_f \rightarrow \mathbf{k}_f'$ gives \mathbf{q}_\parallel which is strictly parallel to \mathbf{h} ("q_∥ scan" or "θ-2θ scan"). If α_f is now varied, then the tails of \mathbf{q} , \mathbf{q}_\parallel , and \mathbf{q}_\perp move slightly along the directions of \mathbf{k}_f' and \mathbf{k}_f'' , as indicated schematically by the heavy marks.

To exhibit the purely geometric features of the cross section, we take a homogeneous defect concentration $\bar{\rho}_D(z) = \bar{\rho}_D$ within the sample. The later comparison with experimental data will be based on a more realistic defect distribution. We choose the relevant ratio of the Lamé constants $\mu/(\lambda + \mu) = 0.5$ and to include absorption we replace $\sin^2 \alpha_c$ by $\sin^2 \alpha_c + i\beta$ in κ with $\beta = -2.5 \times 10^{-7}$.

Figure 3 shows the dependence of the diffuse intensity on α_f/α_c for fixed $|\varphi|$ and $\alpha_i/\alpha_c < 1$ near the (220) reflection in Si with a wavelength of 1.32 Å: curve (a) is

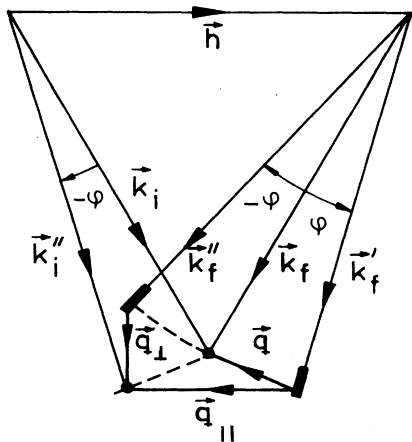


FIG. 2. Scattering geometry in the surface. For further information see text.

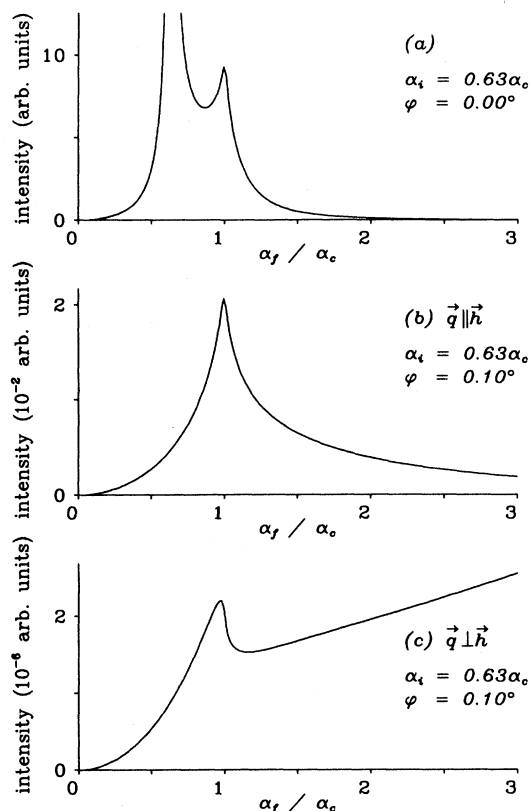


FIG. 3. α_f profiles of the diffuse intensity at the Bragg point ($\mathbf{q} = \mathbf{0}$ if $\alpha_i = \alpha_f$); (a), (b), and (c) for deviation angle $\varphi = 0.1^\circ$ along two different paths in reciprocal space.

for $\varphi = 0$. The strong peak at $\alpha_f = \alpha_i$ occurs in the vicinity of the Bragg reflection, whereas the second lower maximum arises from the strong variation of the penetration depth when $\alpha_f \approx \alpha_c$. The α_f profiles for \mathbf{q}_\parallel and \mathbf{q}_\perp with $|\varphi| = 0.1^\circ$ are displayed by the curves (b) and (c), respectively. Because of $\mathbf{q}_\perp \cdot \mathbf{h} \approx 0$ there is a strong reduction of the intensity in the \mathbf{q}_\perp scan relative to the \mathbf{q}_\parallel scan. In Fig. 4 the q dependence for the \mathbf{q} scan is plotted for different fixed values of α_f . It is noteworthy that the crossover

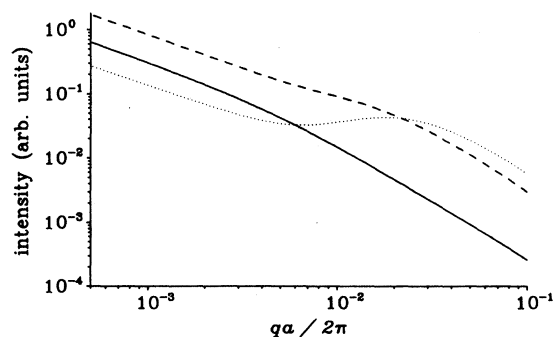


FIG. 4. q dependence of the diffuse intensity in the q -scan mode, with the lattice constant of Si, $a = 5.43$ Å. $\alpha_i = 1.26\alpha_c$. Solid line, $\alpha_f = 0.7\alpha_c$; dashed line, $\alpha_f = 1.0\alpha_c$; dotted line, $\alpha_f = 1.26\alpha_c$.

from the asymptotic $1/q$ regime to the bulk $1/q^2$ behavior is nonmonotonic if both $\alpha_i, \alpha_f > \alpha_c$.

III. EXPERIMENTAL DETAILS AND RESULTS

The samples were perfect Si single crystals of high purity, their surfaces were polished to industrial standard. The normal to the (100) lattice planes formed small angles Ψ with the physical surface of the samples: for sample no. Si-1, Ψ was 0.8 mrad, for sample no. Si-2, Ψ was 1.8 mrad.

Sample no. Si-1 was implanted at ambient temperature with As ions of 80-keV energy to a total dose of $6 \times 10^{13} \text{ cm}^{-2}$. Sample no. Si-2 was the unimplanted reference sample.

The measurements were conducted at the three-axis diffractometer¹¹ at Hamburger Synchrotronstrahlungslabor. The experimental setup is shown in Fig. 5. The synchrotron radiation from DORIS II was monochromized at a plane Ge(111) crystal (M), reflected at a Au-coated mirror (MI), and collimated by slits $S1$ and $S2$. The glancing angle of incidence of the x rays onto the sample (S) was determined by measuring the exit angle of the specularly reflected beam in the counter C behind slit $S5$. The angle α_i was changed by rotation of the sample about the (110) lattice plane normal. The divergence $\Delta\alpha_i$ was 0.3 mrad, the divergence $\Delta\theta_i$ of the incident beam in the scattering plane was 2.9 mrad. The scattered intensity at and near the (220) Bragg reflection was detected in the position-sensitive detector (PSD).

Distributions of diffuse scattered intensity were recorded in two different modes.

" α_f -integrated" spectra were obtained by measuring intensities at different θ_f at one time in the PSD. A slit in front of the PSD allowed the registration of scattered intensity in the range $0 < \alpha_f \leq 2.5\alpha_c$. The admitted divergence $\Delta\theta_f$ in this case was 1.6 mrad (PSD in position A in Fig. 5).

" α_f -resolved" distributions were measured at one fixed

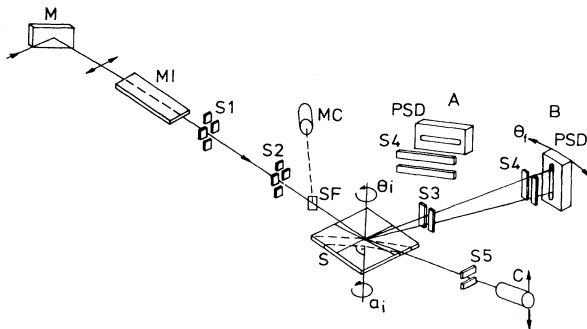


FIG. 5. Experimental setup. M , monochromator; MI , mirror; $S1$ – $S5$, slits; SF , scattering foil; MC : monitor counter; S , sample; PSD , position-sensitive detector; C , counter. For the measurement in the α_f -integrated mode the PSD and $S4$ are rotated by 90° into position A . θ_i : rotation about an axis perpendicular to the sample surface. α_i : rotation about an axis perpendicular to the (220) lattice plane.

position of θ_f , recording intensities at different α_f between $0 < \alpha_f \leq 12\alpha_c$ at one time in the PSD (PSD in position B in Fig. 5). In this mode the divergence $\Delta\theta_f$ was 2.9 mrad, limited by slits $S3$ and $S4$.

Figure 6 shows distributions of scattered intensity in the " α_f -integrated" mode for Si-1 (\circ , implanted), and for Si-2 ($+$, unimplanted), at $\alpha_i = 0.98\alpha_c$. At the wings of the (220) Bragg peak, which is broadened by the resolution function of the experimental setup, diffuse scattered intensity is observed. In the implanted sample it is enhanced and shows a slight asymmetry. The diffuse background intensity in the unimplanted sample—which at least in part is due to thermal diffuse scattering—has to be subtracted in order to obtain the defect-induced diffuse intensity I_D . Since the reference sample had a different misorientation angle Ψ , the correct background intensity at each α_i for the implanted sample was obtained by scaling the spectrum of the unimplanted sample to yield the same integral Bragg intensity as the implanted sample. The validity of this procedure was checked by comparison of measurements on unimplanted samples with different angles Ψ .

As a next step these difference spectra were separated into their symmetric and antisymmetric parts. Here we do not consider the small antisymmetric contribution, but focus on the symmetric part I_D^s :

$$I_D^s(q) := \frac{1}{2}[I_D(+q) + I_D(-q)]$$

which is directly comparable to the results of the theoretical treatment [Eq. (19)]. Figure 7 displays the α_f -integrated distributions of $I_D^s(q)$ for three different values of α_i . One should note that the functional dependence of $I_D^s(q)$ on q , as well as the integral intensities, change characteristically with α_i .

At $qa/2\pi = 1.7 \times 10^{-2}$, α_f -resolved diffuse intensity distributions were recorded for three different values of α_i . Difference spectra were formed in the way described above. Figure 8 shows these α_f -resolved distributions. Within the error of experimental determination of α_f the exit angle α_f^{\max} of the intensity maximum was equal to α_c ,

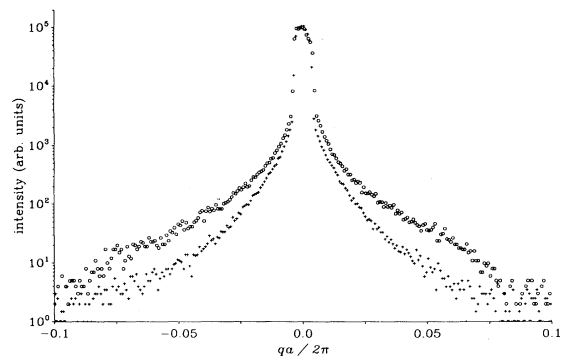


FIG. 6. Diffuse intensity distribution around the (220) Bragg reflection in the α_f -integrated mode for Si-1 (\circ , implanted with 80-keV As ions to $6 \times 10^{13} \text{ cm}^{-2}$), and for Si-2 ($+$, unimplanted), for $\alpha_i = 0.98\alpha_c$.

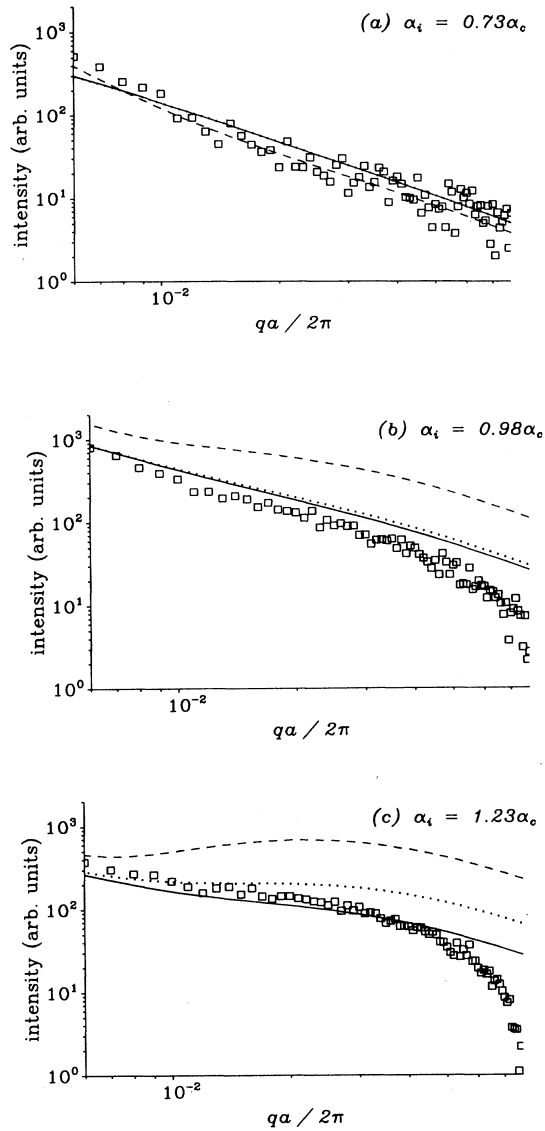


FIG. 7. Symmetric part of the defect-induced diffuse intensity I_D^s in the α_f -integrated mode for three different angles of grazing incidence α_i as indicated. Also shown are theoretical distributions with different defect densities $\bar{\rho}_D(z)$ (see Fig. 9): solid line, defect density II; dotted line, defect density I; dashed line, defect density III.

and we shifted the experimental intensity distributions in α_f to yield $\alpha_f^{\text{max}} = \alpha_c$ in order to facilitate the comparison with theoretical results. While the functional dependence of I_D^s on α_f does not vary appreciably with α_i , the peak height clearly does.

IV. DISCUSSION

Experiments were compared to results of the theoretical treatment presented in Sec. II. For three different defect densities $\bar{\rho}_D(z)$ —shown in Fig. 9—the defect-

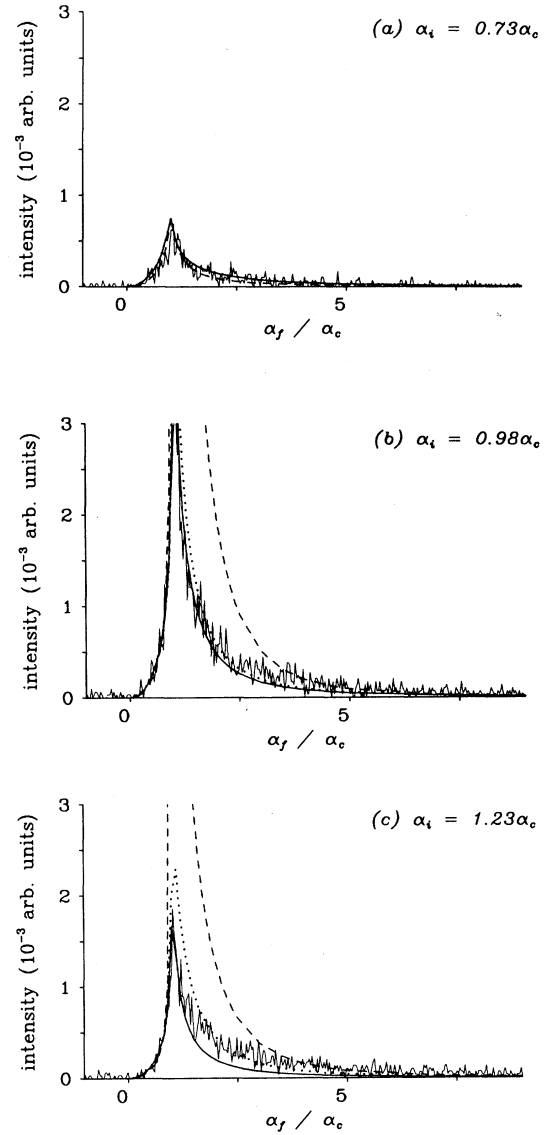


FIG. 8. Symmetric part of the defect-induced diffuse intensity I_D^s in the α_f -resolved mode for three different angles of grazing incidence α_i as indicated, at $\varphi = 0.24^\circ$. Also shown are theoretical distributions with different defect densities $\bar{\rho}_D(z)$ (see Fig. 9). Solid line, defect density II; dotted line, defect density I; dashed line, defect density III.

induced scattered intensities were calculated. Defect density I is a constant density, densities II and III were chosen according to the results of a TRIM (Ref. 12) Monte Carlo simulation: density II corresponds to the dependence on the depth z of the nuclear collisional energy deposited by the incident ion, density III to the distribution of the implanted As ions (which are essentially immobile at the implantation temperature). The validity of TRIM simulations was confirmed repeatedly by Rutherford-back-scattering (RBS) or transmission-electron-microscopy (TEM) experiments (for a recent review see Ref. 13) after implantation to high doses, or after implan-

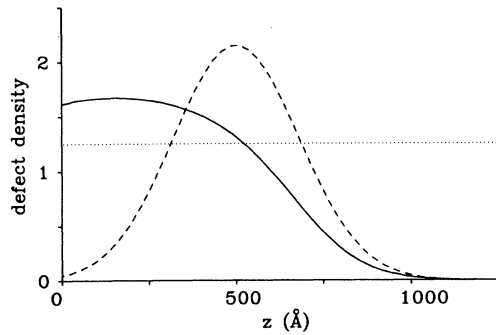


FIG. 9. Defect densities used in the theoretical calculations. Dotted line: defect density I (constant density). Solid line, defect density II, which corresponds to the dependence on z of the nuclear collisional energy deposited by the incident ion; dashed line, distribution in z of the implanted As ions. The functional dependence of densities II and III on z was chosen according to a TRIM Monte Carlo simulation (Ref. 12).

tation and annealing. To our knowledge no experimental information on the defect distribution from TEM or RBS measurements is available after low-dose (6×10^{13} As/cm²) implantation with 80-keV As ions. For each defect density the theoretical spectra for all three different α_i were scaled by one unique factor. It was chosen by a least-squares fit of the theoretical spectra to the experimental distributions for $\alpha_i = 0.73\alpha_c$.

The theoretical curves are given in Figs. 7 and 8 along with the experimental results, α_f -integrated theoretical curves were obtained by numerically integrating theoretical distributions in the range of $0 < \alpha_f \leq 2.5\alpha_c$. Agreement is best for defect density II. In the α_f -integrated mode the functional dependence of I_D^s on q , and its characteristic changes with α_f , are reproduced satisfactorily. Small but significant deviations occur at the smallest q values—probably caused by Bragg contributions, and at large q for $\alpha_i \geq \alpha_c$. The scaled intensities disagree at $\alpha_i = 0.98\alpha_c$. This may be due to the fact that near $\alpha_i = \alpha_c$, intensities vary sensitively with α_i , so that the experimental error in the absolute determination of α_i ($\Delta\alpha_i \approx 0.04\alpha_c$ for this particular measurement) may have appreciable influence. In the α_f -resolved mode we find satisfactory agreement at all angles α_i , except for small deviations in the dependence of I_D^s on α_f at $\alpha_i, \alpha_f > \alpha_c$.

Results for defect densities I and III are inferior. For defect density I at $\alpha_i = 1.23\alpha_c$, calculated intensities are clearly too high [Figs. 7(c) and 8(c)]. Results for defect density III disagree with experiment with respect to the dependence of I_D^s on q and on α_i at $\alpha_i = 0.98\alpha_c$ and at $\alpha_i = 1.23\alpha_c$. The observed deviations may be understood in a qualitative way. Defect density I is too high at large z , and thus causes too high a diffuse intensity at $\alpha_i > \alpha_c$. Defect density III is too small at small z , and produces only small diffuse intensity at $\alpha_i < \alpha_c$. Since intensities were scaled for the measurement at $\alpha_i = 0.73\alpha_c$, overly high scaled intensities result for $\alpha_i \geq \alpha_c$.

The satisfactory agreement of experiment with theory encourages us to conclude that implantation produces

lattice defects that cause appreciable distortion of the host lattice. Their distribution coincides approximately with the distribution of deposited collisional energy.

The theoretical treatment is based on some major assumptions: (i) the defects act as pure dilation centers; (ii) the scattered intensity can be described within the Huang-scattering approximation, and (iii) the defects are arranged in space in an uncorrelated way. The degree to which these assumptions are fulfilled in our real situation will now be briefly discussed.

(i) The single measurement along the path in reciprocal space (q scan, see Fig. 2)—which roughly coincides with a direction parallel to the reciprocal-lattice vector—is not sensitive to the presence of nondiagonal terms in the dipole-force tensor of the defects. Future measurements will explore several different paths in reciprocal space (e.g., will realize q_{\parallel} or q_{\perp} scans), and thus will enable us to identify the symmetry of the displacement field of the defects, as well as allow a more detailed verification of theoretical predictions.

(ii) The Huang approximation is applicable as long as the condition $\mathbf{Q} \cdot \mathbf{u} \ll 1$ is fulfilled. That is the case for most kinds of defects at small enough $|\mathbf{Q}|$. Mayer and Peisl¹⁴ measured defect-induced diffuse scattering after fast-neutron irradiation at room temperature in bulk Si single crystals. Since the mean damage energy due to fast reactor neutrons is comparable to that due to 80-keV As ions, the resulting damage pattern should be comparable. The authors observed Huang scattering—with the characteristic bulk $1/q^2$ dependence—up to $qa/2\pi = 6 \times 10^{-2}$ near the (440) reflection, and deviations from this behavior at larger q . The discrepancy between our experimental spectra and theory for $qa/2\pi > 5 \times 10^{-2}$ [cf. Figs. 7(b) and 7(c)] possibly arises in the same way from the influence of strong distortions in the vicinity of the defects. These distortions may also cause the small antisymmetric contributions to the defect-induced diffuse intensity.

(iii) Since defects are produced by ion irradiation in a correlated way (in defect “cascades”), one expects them to be arranged in agglomerates, possibly in the form of dislocation loops. After reactor-neutron irradiation,¹⁴ evidence for the presence of small agglomerates of interstitials and vacancies was found. This correlation will result in an enhancement of I_D by a constant factor at small enough q , where the condition $qR_c < 1$ is fulfilled (R_c is the spatial extent of the correlation). Since in this q range the functional dependence of I_D on q remains unchanged, the neglect of defect correlations appears to be justified.

The theoretical treatment contains some further simplifications, e.g., an isotropic medium is assumed, and the change of elastic constants near the surface is neglected. The comparison with experimental results shows that within these approximations the gross features of the experimental data for small values of q are reproduced satisfactorily.

The investigation of near-surface defects by measurement of diffuse scattering under conditions of grazing incidence and exit promises to be of considerable practical importance. The method is nondestructive, and allows

the study of structure, symmetry, and strength of various types of defects, as well as of their distribution with the distance from the surface. Defect correlations and changes in the defect structure during thermal annealing treatment can be observed. Only in some instances are there complementary methods which can give comparable information, as cross-sectional TEM (a destructive method) for the study of two-dimensional defect structures, or channeling for low concentrations of single defects.

In order to fully exploit the potentialities of the method, future measurements will improve and expand these first experiments. The structure and symmetry of defects will be studied by determining several different appropriate combinations of components of the dipole-force tensor. To this end, measurements in different directions in reciprocal space are necessary. The dipole-force tensor in absolute units can be determined by normalization of scattered intensities in terms of the incident intensity.

Detailed information on the defect distribution is contained in the dependence of $I_D^s(q)$ on α_i and α_f . In this context the apparent insensitivity of the functional dependence of $I_D^s(q)$ on α_f should be considered. It is caused by the fact that the defect density present (compare Fig. 9) varies slowly with z compared to the exponential damping of the fields. In this case detailed information on $\bar{\rho}_D(z)$ can be extracted only by careful analysis of high-resolution data. The significant enhancement of the experimental above the theoretical curve at α_i and α_f larger than α_c [see Fig. 8(c)] can be explained by a higher actual defect density at large z compared to

density II. In view of the limited amount of experimental information, however, we yet refrain from an independent determination of $\bar{\rho}_D(z)$: more experimental data at $\alpha_i > \alpha_c$, where the behavior of I_D^s with q and α_f depends sensitively on $\bar{\rho}_D(z)$, are required.

The scope of the theoretical treatment will be expanded to include also strong distortions in the vicinity of defects. A significant improvement of the agreement with experiment is expected concerning the behavior at large q and the antisymmetric contributions. The elastic anisotropy of the host crystal can be taken into account explicitly in numerical calculations.

V. SUMMARY

We have presented the theory of Huang diffuse scattering under conditions of grazing incidence and exit. The first experiments essentially confirm the predictions of theory. They allow the determination of the depth distribution of defects, induced in Si single crystal by implantation with 80-keV As ions. The method applied promises to be of considerable importance for the study of the real structure of solids near their surface.

ACKNOWLEDGMENTS

We are indebted to N. Bernhard, who assisted in the initial stages of the experimental work, and to H. Kakoschke (Siemens A.G., München), who supplied the implanted sample. This work has in part been funded by the German Federal Ministry for Research and Technology under Contract No. 03PE1LMU/2.

¹H. Trinkaus, Z. Naturforsch. **28a**, 980 (1973); P. H. Dederichs, J. Phys. F **3**, 471 (1973).

²S. Dietrich and H. Wagner, Z. Phys. B **56**, 207 (1984).

³B. C. Lu and S. Rice, J. Chem. Phys. **68**, 5558 (1978).

⁴W. C. Marra, P. Eisenberger, and A. Y. Cho, J. Appl. Phys. **50**, 6927 (1979).

⁵G. Wallner, E. Burkel, H. Metzger, and J. Peisl, Phys. Status Solidi A **88**, 505 (1985).

⁶P. A. Aleksandrov, A. M. Afanasev, A. L. Golovin, R. M. Imamov, D. V. Novikov, and S. A. Stepanov, J. Appl. Crystallogr. **18**, 27 (1985).

⁷H. Dosch, L. Mailänder, A. Lied, J. Peisl, F. Grey, R. L. Johnson, and S. Krummacher, Phys. Rev. Lett. **60**, 2382 (1988).

⁸Z. G. Pinsker, *Dynamical Scattering of X-rays in Crystals* (Springer, Berlin, 1978).

⁹N. Bernhard, E. Burkel, G. Gompper, H. Metzger, J. Peisl, H. Wagner, and G. Wallner, Z. Phys. B **69**, 303 (1987).

¹⁰M. A. Krivoglaz, *Theory of X-Ray and Thermal Neutron Scattering by Real Crystals* (Plenum, New York, 1969).

¹¹J. Als-Nielsen and P. S. Pershan, Nucl. Instrum. Methods **208**, 545 (1983).

¹²J. P. Biersack and L. G. Haggmark, Nucl. Instrum. Methods **174**, 257 (1980).

¹³K. S. Jones, S. Prussin, and E. R. Weber, Appl. Phys. A **45**, 1 (1988).

¹⁴W. Mayer and J. Peisl, J. Nucl. Mater. **108/109**, 627 (1982).